Multiple scattering of seismic waves in a heterogeneous magmatic system and spectral characteristic of long period volcanic earthquakes

- Mirko Bracale[1]: mirko.bracale@univ-grenoble-alpes.fr
- Michel Campillo[1]: michel.campillo@univ-grenoble-alpes.fr
- Nikolai M. Shapiro[1]:nikolai.shapiro@univ-grenoble-alpes.fr
- Romain Brossier[1]: romain.brossier@univ-grenoble-alpes.fr
- Oleg Melnik[2]: oemelnik@gmail.com

[1]ISTerre, Université Grenoble Alpes, CNRS, Université Savoie Mont Blanc, IRD, Université Gustave Eiffel, Grenoble, France

[2]Department of Earth Sciences, University of Oxford, Oxford, UK

Multiple scattering of seismic waves in a heterogeneous magmatic system and spectral characteristic of long period volcanic earthquakes.

Mirko Bracale[1], Michel Campillo[1], Nikolai M. Shapiro[1], Romain Brossier[1], Oleg Melnik[2]

[1]ISTerre, Université Grenoble Alpes, CNRS, Université Savoie Mont Blanc, IRD, Université Gustave Eiffel, Grenoble, France
[2]Department of Earth Sciences, University of Oxford, Oxford, UK

Key Points:

- keypoint 1.
- keypoint 2.
- keypoint 3.

Corresponding author: Nikolai Shapiro, `Nikolai.Shapiro@univ-grenoble-alpes.fr`

Abstract

Long-Period (LP) volcanic earthquakes are characterized by a relatively long duration codas and spectra containing pronounced spectral peaks. These peculiar spectral characteristics are often attributed to source effects, such as resonances of fluid-filled cracks. In this paper, we report the results of numerical simulations of seismic wave propagation showing that the main signal features of the LP earthquakes (long duration and spectral peaks) can arise from strong multiple scattering in the strogly heterogeneous volcanic media. We consider seismic sources located within a strongly heterogeneous volcanic plumbing system created through multiple injections of magmatic dykes and sills into the surrounding crustal rocks. The resulting structure is characterized by multiple batches of almost fully melted rocks and, as a consequence, by very strong contrasts of elastic properties. By computing the propagation of waves in this medium, we show that the highly heterogeneous structure generates strong multiple scattering of seismic waves, whose interference leads to multiple peaks in the signal spectra. Some of these peaks are common to multiple receivers and thus are produced by local resonances in the vicinity of sources located in areas where the media is particularly heterogeneous. Although arising within irregular-shaped magma batches, these local resonances have a similarity with the fluid-filled crack model, implying that their frequencies are somehow linked to the near-source structure. Meanwhile, many spectral peaks are observed only for specific source-receiver pairs, implying that they are due to the interference of waves traveling along specific paths and therefore should not be interpreted as signatures of the near-source structure and processes. Overall, our results show that separating path and source effects for seismo-volcanic signals in realistically heterogeneous media might be delicate and not all spectral features should be attributed to the latter.

1 Introduction

Volcano seismology is one of the main sources of information about the structure of magmatic plumbing systems and ongoing physical processes occurring at depth beneath volcanoes. Active volcanoes are associated with a variety of seismic signals (e.g., B. A. Chouet & Matoza, 2013). Seismic signals are mathematically described as a convolution of source and propagation terms (Aki & Richards, 2002). The latter term called the Green's function is related to the structure of the media through which the seismic waves propagate. The source term is directly related to active processes within volcano magmatic systems, i.e., stress releases, magma motion, degassing, etc. Many seismovolcanic studies approximate the Green's function by assuming a nearly homogeneous medium, sometimes incorporating topography and smooth large-scale variations. Under this assumption, the complexity of recorded seismic signals and their spectra is primarily attributed to the source process.

An example of using the above mentioned approximation is the approach often adopted to study the long-period (LP) volcanic earthquakes (e.g., B. A. Chouet, 1996). The respective signals are characterized by relatively long codas and are weakened in high frequencies compared to small tectonic earthquakes of similar sizes. The peculiar spectral properties of the LP volcanic seismicity include the existence of narrow spectral peaks that often remain very stable in time for swarms of earthquakes or long-lasting seismic tremors. The origin of such a spectral behavior is often attributed to possible source mechanisms, which still remain elusive and debated. Many of the suggested models link the origin of the LP seismicity to fluid pressure variations occurring in the plumbing system: fluid-driven cracking (Aki et al., 1977), resonances of fluid-filled cracks (B. Chouet, 1986, 1988), non-stationary magma flux (Julian, 1994), magma-wagging oscillation (Jellinek & Bercovici, 2011), percolation of gases through a permeable layer (Girona et al., 2019), magma–hydrothermal coupling (Matoza & Chouet, 2010), and rapid gas bubble growth in magma (O. Melnik et al., 2020, 2024). Alternatively, the origin of LP volcanic earthquakes has been attributed to stick-slipping of viscous magmas (Iverson et al., 2006) or to slow rupture within volcanic edifices (Bean et al., 2014).

The LP earthquakes are often interpreted in the framework of the fluid-filled crack model (e.g., B. Chouet, 1986, 1988) when the source duration and spectrum are controlled by resonances of this fluid filled structure. In the case of simple rectangular crack, the resonance frequencies can be described with an empirical analytical equation (Maeda & Kumagai, 2013, 2017). By neglecting propagation effects, this solution enables a direct interpretation of the peak frequencies observed in recorded spectra in terms of the size and mechanical properties of the resonating crack.

The model considering a single regularly-shaped crack embedded in a perfectly homogeneous medium represents a very strong simplification of a real volcano-plumbing system. The real volcanic media are strongly heterogeneous. A clear manifestation of this heterogeneity is the strong scattering of seismic waves expressed in enhanced codas of many seismo-volcanic signals (e.g., Wegler & Lühr, 2001; Wegler, 2003; Del Pezzo, 2008; Yamamoto & Sato, 2010; Obermann et al., 2014; Chaput et al., 2015; Blondel et al., 2018). Therefore, the propagation of seismic waves within volcano-magmatic systems cannot be accurately described by Green's functions of a transparent medium but must account for small-scale heterogeneity. In particular, interference of multiply scattered waves on this small-scale heterogeneity may affect the spectra of recorded signals at frequencies between 1 and 10 Hz relevant to the source processes of the LP volcanic earthquakes (Barajas et al., 2023).

The relevant spatial scale of heterogeneity comprises objects with sizes between a few kilometers and a few tens of meters. Such small-scale features are very difficult to characterize because high-frequency waveform inversion is strongly complicated by scattering, and seismic tomography produces only very spatially smoothed images (e.g., Koulakov & Shapiro, 2014). In the absence of precise knowledge of the details of the structure at depth, seismic scattering is often described with statistically uniform distribution of small-scale heterogeneities and in the framework of radiative transfer theory (e.g., Aki & Chouet, 1975; Abubakirov & Gusev, 1990; Margerin et al., 1998; Margerin, 2005; Sato et al., 2012) that models the wavefield intensity with ignoring its phase and the wave interference.

In the present work, our aim is to comprehend how the multiple scattering of seismic waves on the small-scale heterogeneity within the volcano-plumbing systems may affect the properties of recorded seismograms and their spectra. In the absence of sufficiently high-resolution images of the volcanic interior, we decided to use a "realistic" medium model of O. E. Melnik et al. (2021) based on modern concepts of formation of volcano magmatic systems. With this clearly non-uniform model, we consider deterministic properties and simulate full seismic wavefields by numerically solving the 2D elastodynamic equations with a spectral element method (Komatitsch & Vilotte, 1998; Trinh et al., 2019; Cao et al., 2022).

In the following sections, we first describe the heterogeneous model of the magmatic plumbing system. Then, we focus on the technical aspects of the numerical simulations and on the preliminary analyses aimed at ensuring the reliability of our synthetic data. In a second time, we analyze the synthetic signals and their spectra. In particular, we focus on understanding the origin of multiple spectral peaks and investigate their stability with respect to the source and receiver positions. We conclude that frequencies of these peaks are not controlled by the source function but by the complex wave propagation that sometimes results in local resonances related to particularly strong contrasts of media properties in the vicinity of the sources.

2 Model of heterogeneous magmatic plumbing system

Large magmatic reservoirs in the crust are believed to be built by long-term replenishment from higher depths with the repetition of multiple small-volume intrusions in the form of sills and dikes (Annen et al., 2005; Cashman et al., 2017; O. E. Melnik et al., 2021). Each intrusion supplies both thermal energy and molten material. Its emplacement is followed by interaction with the host rocks with their partial melting and by cooling and partial crystallization of the magma. After continuing for several thousand years, this process results in a very heterogeneous structure of the affected part of the crust with many small nearly fully molten pockets of irregular shape embedded in solid rocks. The overall temperature anomaly, the total amount of melt in the system, and the degree of spatial heterogeneity depend on the history of magma emplacement, i.e., on its duration and average intrusion rate.

The above-mentioned concept of the formation of large magma reservoirs is physically modeled by O. E. Melnik et al. (2021) in 2D. This model considers many episodes of almost instantaneous emplacements of intrusions of elliptical shape with thicknesses varying between 10 and 20 m and lengths varying between 200 and 1500 m. The positions and orientations of these intrusions are randomly distributed in space to mimic the emplacement of sills and dikes (nearly horizontal and vertical orientations, respectively). The intrusion times are set according to their volumes to follow the imposed magma injection rate. A system of equations that accounts for advection due to magma and rock displacement, heat conduction, and latent heat of crystallization is then numerically solved. As an output of the modeling, 2D distributions of temperature, melt fraction, composition, and density are obtained. In the next step, effective elastic moduli and seismic velocities of partially molten rocks are computed using the method of Schmeling et al. (2012).

In this study, we use the thermo-compositional model presented in Figure 5 of O. E. Melnik et al. (2021). The 10 × 10 × 10 km magmatic reservoir (the third spatial dimension is the horizontal "depth" of all intrusions) has been formed by injection of basaltic intrusions into the granitic crust during 75 ka with the rate of 0.25 m^3/s. We then used the 2D distributions of density $\rho(x, z)$ and seismic velocities $V_P(x, z)$ and $V_S(x, z)$ predicted from this model to simulate the propagation of seismic waves. We made a specific adaptation of the V_S distribution to be able to use it in the framework of elastic wave propagation. In areas where the melt fraction approaches 1, the S-wave velocity reduces to close to 0 m/s, causing numerical instabilities. To address this, we introduced a minimum S-wave velocity of 200 m/s, ensuring the stability of the computations.

The resulting structure of the elastic medium is very heterogeneous with many small-scale features characterized by strong velocity contrasts (V_S ranging from 200 to 3500 m/s) as shown in Figure 1a. The average values of P- and S-wave velocities and density are $5.5km/s$, $3.2km/s$, and $2300kg/m^3$ respectively.

In this study, we focus on the wave scattering caused by the heterogeneity within the magmatic plumbing system. Therefore, we neglect the near-surface wave scattering. This latter can be caused by the very complex structure of volcanic edifices and also by the the topography of the volcano, although both are expected to add additional complexity to the seismo-volcanic wavefields (e.g., Ripperger et al., 2003).

To characterize the strength of the velocity fluctuations, we compute the normalized standard deviation of the shear wave velocity:

$$\epsilon(x, z) = \frac{\sigma_S}{\langle v_s \rangle_S} = \frac{\sqrt{\frac{1}{N} \iint\limits_S (v_s(\tilde{x}, \tilde{z}) - \langle v_s \rangle_S)^2 d\tilde{x} d\tilde{z}}}{\langle v_s \rangle_S} \tag{1}$$

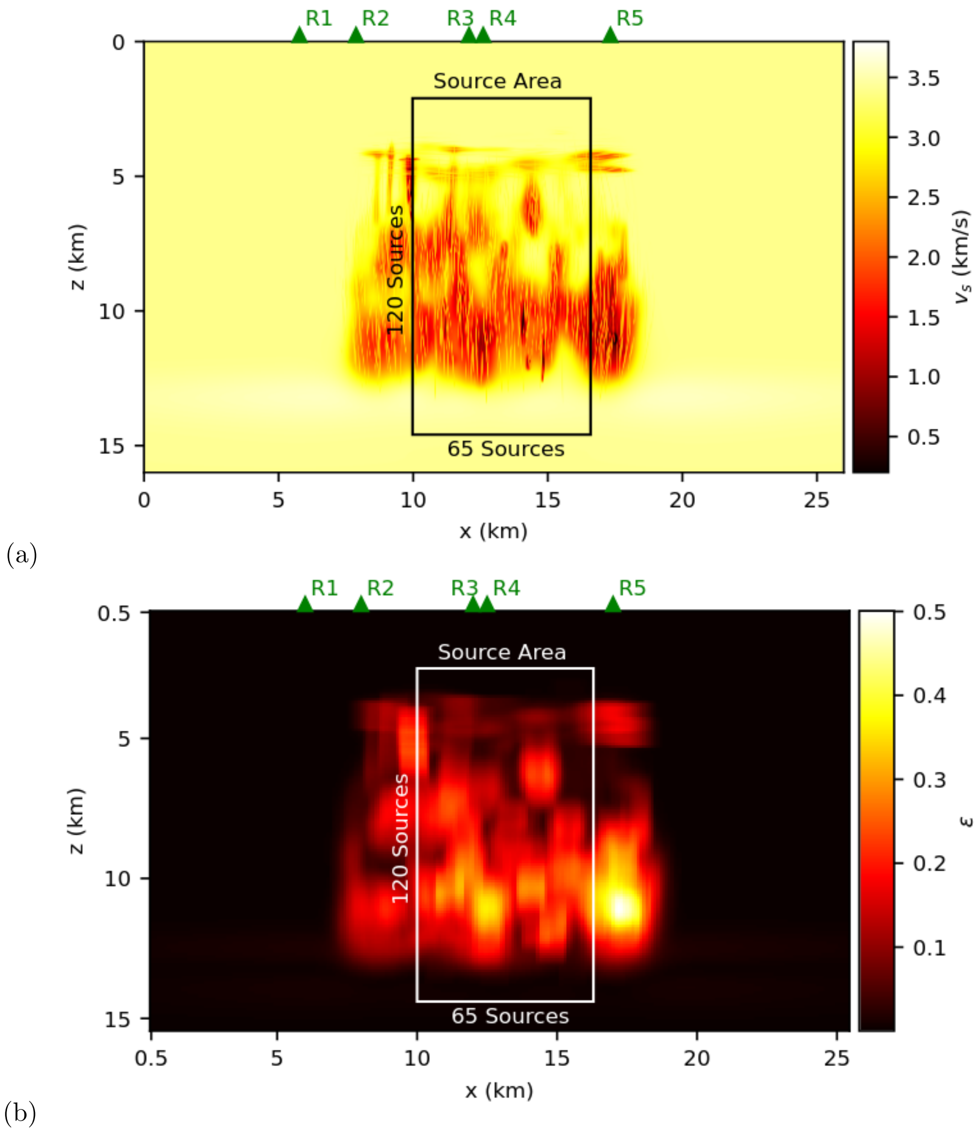

Figure 1. Synthetic seismic velocity model. (a) Shear wave velocity. (b) standard deviation of the shear wave velocity fluctuations (equation 1).

where σ_S is the standard deviation of the velocity model computed over the area S, and $\langle v_s \rangle_S$ is the average velocity in the same area. The area S is a square of size l = 1 km centered at the point (x, z). The spatial distributions of ϵ, shown in Figure 1b, demonstrate that the model exhibits pronounced non-uniformity in the distribution of heterogeneity. The uppermost layer, which extends to a depth of approximately 4 km, is homogeneous. In contrast, the region between depths of 4 and 6 km contains numerous sills, marked by velocity fluctuations (ϵ) ranging from 20% to 30%. Below this, the structural complexity increases further because of the presence of dykes. These sills and dykes are characterized by minimum S-wave velocities as low as 200 m/s and.

In contrast to theories describing the scattering of waves in media with laterally homogeneous distribution of the scattering parameters (e.g., Sato et al., 2012), the model of synthetic plumbing system considered in our study is highly non-uniform. This non-uniformity leads to spatially varying scattering properties, implying that the classical scattering parameters are not meaningful descriptors of the overall scattering process. Therefore, to understand its properties, we carry out a set of numerical experiments based on full elastic wave propagation, as described in the following sections.

3 Numerical simulations of 2D elastic wave propagation

In this study, we numerically solve the elastodynamic equations with the 2D spectral element method implemented in the simulation code SEM2D (Trinh et al., 2019; Cao et al., 2022). This code has been validated for heterogeneous media in previous research where SEM simulations were compared to radiative transfer equation predictions. For the full discussion refer to Bracale et al. (2024, Chapter 3). Because of the strong structural heterogeneity of the model used and extreme velocity contrasts, simulating long signals remains extremely challenging for several reasons.

First, computational costs present a significant challenge. Simulation of wave propagation within a highly heterogeneous structure requires a large number of small elements, which in turn necessitate small time steps. Moreover, the strong multiple scattering results in a long coda of seismograms whose simulation requires an extended simulation time. Together, these factors impose a substantial computational burden.

Second, the boundary conditions at the edges of the medium significantly influence the simulation output. Absorbing boundaries are particularly critical, as they prevent edge reflection artifacts by absorbing the energy that propagates toward the model's edges. To sufficiently attenuate these edge reflections and avoid their interference with the multiply scattered waves on the small-scale heterogeneity, we used 4.5km thick absorbing region (Figure S1).

The final model is composed by 5200x3200 square elements with a side length of 5 meters, along with 900 additional elements composing the absorbing boundaries. The top surface of the model was set to have a free surface boundary condition. Therefore, the total dimensions of the model are 26x16 kilometers, or 35x20.5 kilometers including the absorbing boundaries.

Given the size of the model and the length of the signal to be generated, an interpolation order of 2 was chosen to simplify the calculations. This choice is justified by the fact that the wavelengths associated with the studied frequencies are at least 20 meters long, which corresponds to approximately 4 elements. The synthetic seismograms are bandpass filtered between 1 and 10 Hz. The lower limit is set due to the effects of the absorbing boundaries, while the upper limit is determined by the element size and the interpolation order.

An example of simulated wavefield for a source located at the surface is shown in Figure 2. Outside the area affected by the intrusions, the media is "transparent" and the wavefield is dominated by direct ballistic P and S waves. Withing the magma containing zone, the strong scattering emerges after arrival of direct P and, especially, S waves (snapshots at 2.5 and 3.5 s, respectively). As a result, the wavefield is "randomized" and a significant portion of the wave energy remain "trapped" in the heterogeneous region for long time.

We consider 7800 sources sources located within or in the vicinity of the plumbing system and 5 receivers located at the surface (Figure 1). Position of the receivers are:

$$\begin{aligned} \xi^r_k = [x^r_k, z^r_k] \quad k = 0, 4 \\ x^r_0 = 6.0\,km\ x^r_1 = 8.0\,km\ x^r_2 = 12.0\,km\ x^r_3 = 12.5\,km\ x^r_4 = 17.0\,km \\ z^r_k = 0\,km \end{aligned} \tag{2}$$

The sources are arranged on a regular grid with a 100 m spacing. Their positions are:

$$\begin{aligned} \xi^s_{i,j} = [x^s_{i,j}, z^s_{i,j}] \quad i = 0, 65 \quad j = 0, 120 \\ x^s_{i,j} = 10 + 0.1\,i\,km \quad z^s_{i,j} = 2.5 + 0.1\,j\,km \end{aligned} \tag{3}$$

3.1 Accelerating calculations based on the reciprocity theorem

At each respective location, we need to simulate single force sources in vertical and horizontal directions. The source-time function $S(t)$ is a Ricker wavelet with the central frequency of 3 Hz. The resulting $5 \times 2 \times 7800$ synthetic seismograms are convolutions of the source-time function with the respective Green's functions. So far, displacement u at component n recorded by receiver k excited by a force in direction m and acting at a source position i, j (see equations 2 and 3) can be written as:

$$u_{n,m}(\xi^r_k, t; \xi^s_{i,j}) = S(t) * G_{n,m}(\xi^r_k, t; \xi^s_{i,j}) \tag{4}$$

where G are the Green's function, and t is time from origin.

To reduce computation time, instead of running 2×7800 simulations presumed by equations (4), we compute 2×5 reciprocal wavefields:

$$\tilde{u}_{m,n}(\xi^s_{i,j}, t; \xi^r_k) = S(t) * G_{m,n}(\xi^s_{i,j}, t; \xi^r_k) \tag{5}$$

excited by sources at 5 receiver positions and recorded at all 7800 source positions. We then use the elastodynamics reciprocity theorem (Aki & Richards, 2002) to retrieve the direct wavefields:

$$\begin{aligned} G_{n,m}(\xi^r_k, t; \xi^s_{i,j}) = G_{m,n}(\xi^s_{i,j}, t; \xi^r_k) \\ u_{n,m}(\xi^r_k, t; \xi^s_{i,j}) = \tilde{u}_{m,n}(\xi^s_{i,j}, t; \xi^r_k) \end{aligned} \tag{6}$$

An example of comparison of direct and reciprocal seismograms is shown in Figure S2. All simulation parameters are presented in Table 1.

4 Results: analysis of synthetic seismograms

Examples of synthetic seismograms generated by sources at four different depths are shown in the left frames of Figure 3. For two sources located above the magma storage area (depths of 2.5 and 4.5 km), signals are strongly dominated by ballistic P and S waves. For sources located within the heterogeneous region containing many intrusions

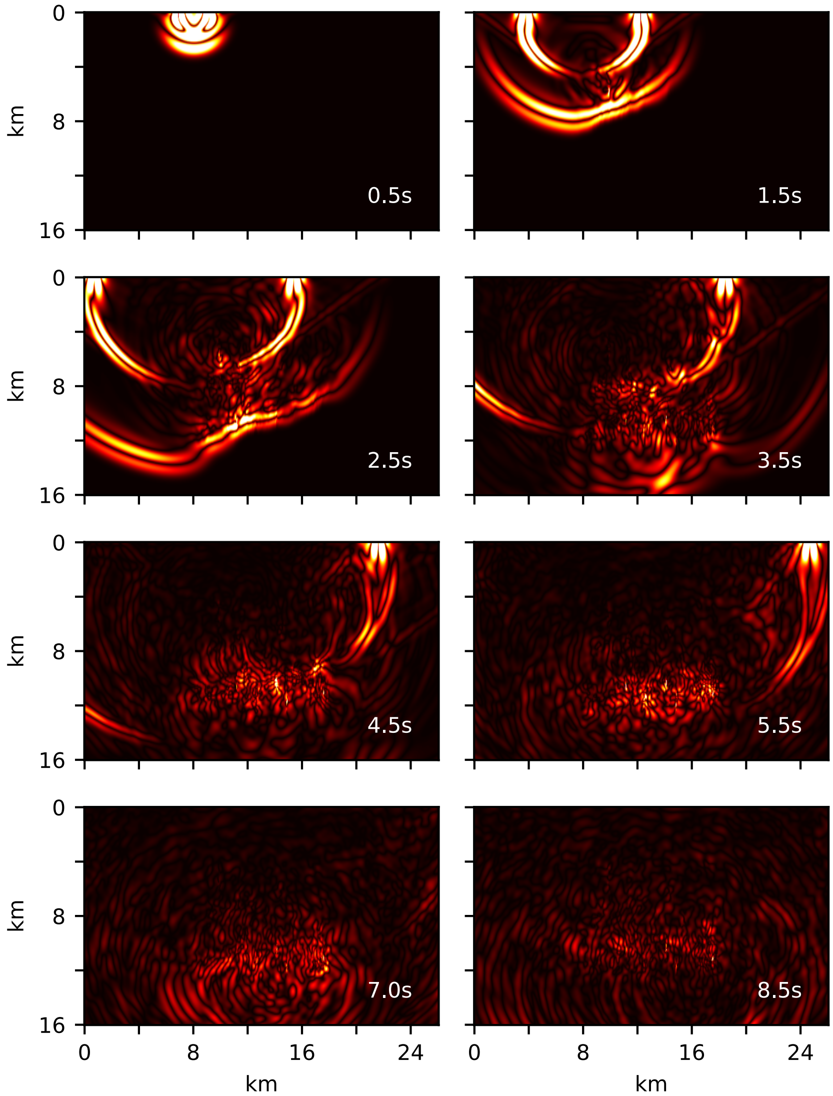

Figure 2. Snapshots of the vertical displacement wavefield amplitude generated by a vertical force source located at x=8.0km, z = 0km. Times after origin are indicated at bottom-right corners of the snapshots.

Parameter	Value
Elements number	5200x3200
Elements size	$5m$
Source function	Ricker - $3Hz$
Absorbing boundary elements	900
Interpolation order	2
Simulation time	37.4 s
Time step	2.5e-4s

Table 1. Settings of the simulation.

(depths of 7.5 and 11.5 km), a strong coda appears after ~ 5 s. This observation is similar to what can be seen in the example of wavefiled snapshots (Figure 2). When the medium between the source and the receiver does not exhibit strong heterogeneity, the scattering of waves and the resulting coda are weak. In contrast, the strong scattering and coda emerge for sources surrounded by the media heterogeneity. In the Fourier domain, the latter scattered arrivals "interfere" with the ballistic waves, resulting in many narrow peaks in the amplitude spectra (middle frames of Figure 3).

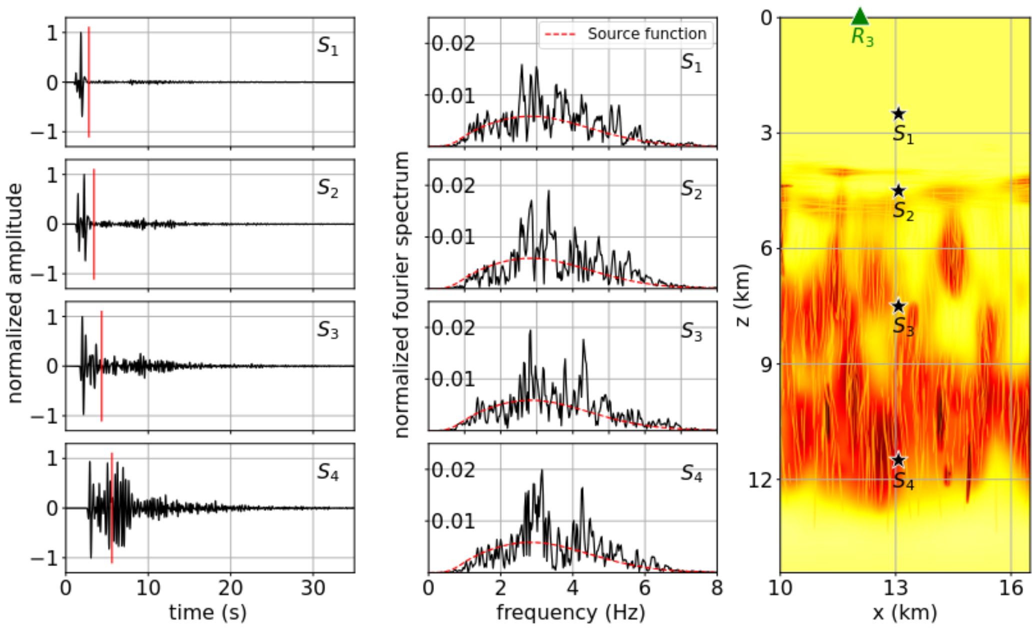

Figure 3. Vertical displacement seismograms (left frames) and their Fourier amplitude spectra (right frames) recorded at receiver number 3 (x=12.5km) generated by four vertical force sources located at x = 13.0km and different depths: $z_{S_1} = 2.5\,km, z_{S_2} = 4.5\,km, z_{S_3} = 7.5\,km, z_{S_4} = 11.5\,km.$ Dashed red lines show the spectrum of the source time function.

To illustrate that the complexity of the spectrum is primarily due to the scattering, we compare, in Figure 4, the amplitude spectra computed from the ballistic waves and the coda for all sources and receiver number 3. We define the ballistic window as the time interval between $t = 0$ (source origin) and the end of ballistic S-wave that would propagate in a homogeneous medium :

$$t_{coda}(x_s, z_s; x_r, z_r) = \frac{\sqrt{(x_s - x_r)^2 + (z_s - z_r)^2}}{\langle v_s \rangle} + t_{sf} \tag{7}$$

Here $[x_s, z_s]$ and $[x_0, z_0]$ represent the locations of source and receiver, respectively. $\langle v_s \rangle$ is the average S-wave velocity of the entire model, and t_{sf} is the duration of the source function, $2s$. The coda window is defined as the time interval from the end of the ballistic window to the end of the seismogram (37.4 s). The times separating ballistic and coda windows are indicated with vertical red lines in the left frames of Figure 3. In 4, we clearly see that the panel with ballistic spectra is significantly smoother in the horizontal direction compared to that of the coda, which exhibits series narrow spectral peaks. The nearly periodic fluctuations of the amplitude in the vertical direction in the left frames are explained by the varying source-receiver distance and geometrical spreading of direct waves.

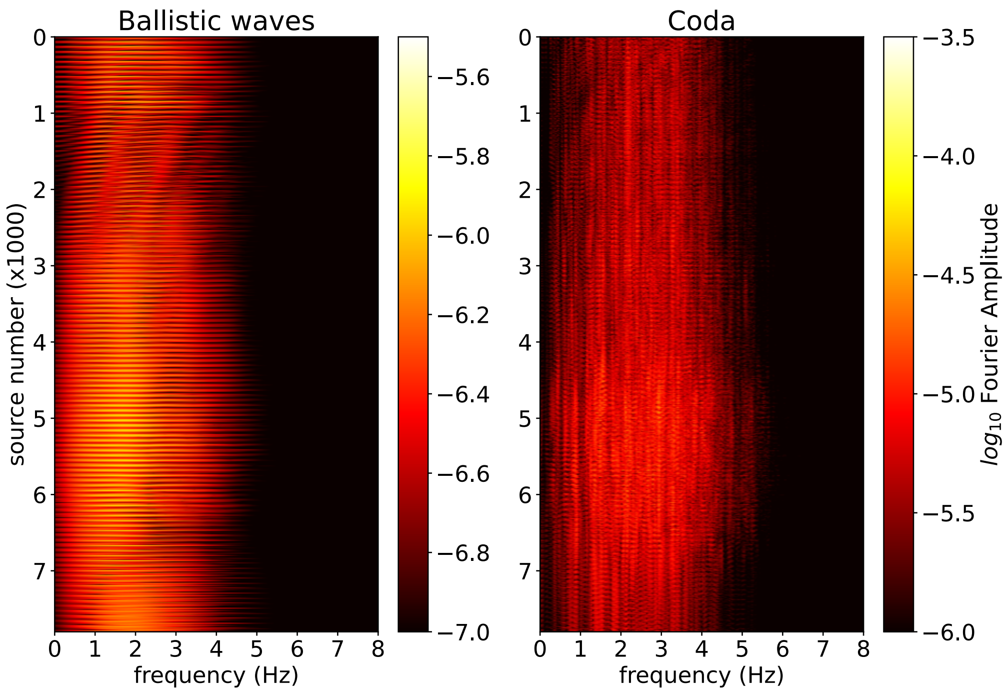

Figure 4. Spectra of vertical displacement generated by a vertical force recorded at receiver number 3 for all the sources, sorted by source number. On the left, the spectrum obtained considering only the ballistic arrivals; on the right, considering only the coda. The ballistic part appears much smoother than the coda part, indicating that the peaks in the signals are related to the waves scattered in the structure.

The inspection of the individual spectra of (Figure 3) reveals that even the source closest to the surface produces a spectrum significantly different from the source function. Numerous observed frequency peaks result from the interference of direct and multiple scattered waves traveling between the source and the receiver. This sum of individual arrivals produces visible interferences in the frequency domain, in the form of spectral peaks. In this case, the peaks observed in the signal spectrum may vary depending on the source and observation point.

4.1 Strength of scattering and media heterogeneity

In Figure 4 we can see some first-order correlation between the media properties and the intensity of scattering expressed in the coda. The spectra of the latter are most intense for sources between 4500 and 7000, i.e., located withing the part of the media most affected by dikes and sills. To investigate this correlation further we compare the strength of the coda with the level of the media heterogeneity in the source region. The former is characterized by the energy of the coda. We start by computing coda energies for individual seismograms. For example, for a horizontal component signal from source $\xi^s_{i,j}$ recorded at receiver ξ^r_k, $u^2_x(\xi^s_{i,j}, \xi^r_k, t)$, the coda energy is computed as:

$$E_c(u_x(\xi^s_{i,j}, \xi^r_k, t)) = \int_{t_{coda}}^{T} \left(u^2_x(\xi^s_{i,j}, \xi^r_k, t) + \mathcal{H}^2\{u_x(\xi^s_{i,j}, \xi^r_k, t)\}\right) dt \tag{8}$$

where $\mathcal{H}$ is the Hilbert transform of the signal. In a next step, the energy fo each source is averaged over two components and all five receivers:

$$\langle E^{i,j}_c \rangle = \frac{1}{5} \sum_{k=1}^{5} (E_c(u_x(\xi^s_{i,j}, \xi^r_k, t)) + E_c(u_z(\xi^s_{i,j}, \xi^r_k, t))) \tag{9}$$

Finally, the energy was normalized by the calculated value for the reference source $\xi^s_{0,0}$, located at $x^s_{0,0} = 10.0$ km and $z^s_{0,0} = 2.5$ km:

$$\langle E^{i,j}_c \rangle_{norm} = \langle E^{i,j}_c \rangle / \langle E^{0,0}_c \rangle \tag{10}$$

The level of heterogeneity is quantified with the media standard deviation (equation 1) computed at the source position. The comparison shown in Figure 5 shows a clear correlation between the logarithm of the coda energy and ϵ.

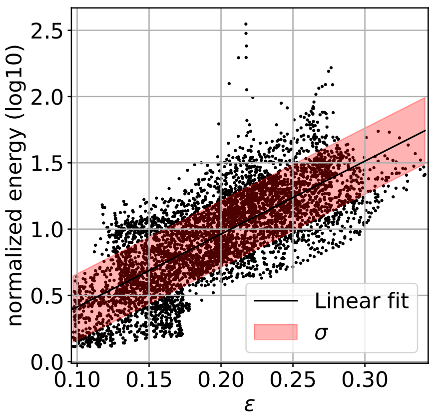

Figure 5. Logarithm of the normalized coda energy as a function of ϵ in the source region for all source-receiver pairs. Vertical component force sources located in points with $\epsilon > 0.1$ were considered.

The spatial distribution of the coda energy as function of the source position for different frequency bands is shown in Figure 6. It can be seen that the strongest coda is generated in the areas characterized by strong media heterogeneity. In particular, the brightest spot of the coda energy at approximately x = 12.5 km, z = 11 km coincides with the large values of ϵ. At low frequencies (Figure 6b) the spatial distribution is relatively smooth and focuses more on some particular structures at higher frequencies (smaller

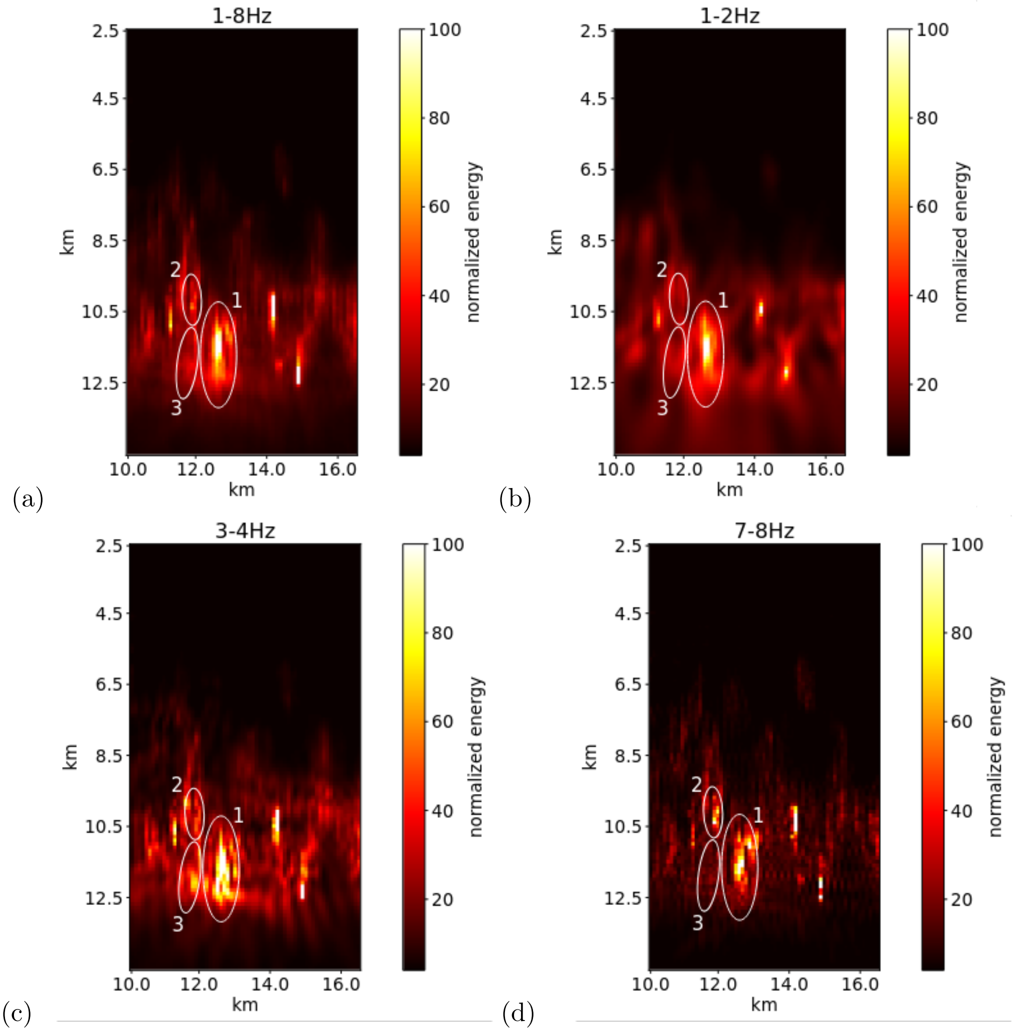

Figure 6. Maps of the normalized coda energy generated by vertical component force sources computed after filtering signals in different frequency ranges: (a) All frequencies, (b) 1-2Hz, (c) 3-4Hz, (d) 7-8Hz.

wavelengths). Another observation concerns the fact that not all areas are activated within the same frequency range. In Figure 6, we have highlighted three areas. The "brightest" Area 1 is seen at all frequencies. Area 2, is mostly visible at high frequencies between 7 and 8 Hz. Area 3 is mostly visible between 3 and 4 Hz. This demonstrates that the frequency content of the coda varies spatially in our strongly non-uniform media and implies that areas with different scattering properties can selectively trap certain wavelengths while allowing other wavelengths to propagate outward.

4.2 Emergence of "local resonances".

The model of B. A. Chouet (1996) suggests that the "stable" peaks in the spectra of LP volcanic earthquakes result from resonances of the fluid-filled cracks, which represent the magmatic intrusions. In this model a single regularly shaped crack embedded in a homogeneous elastic medium is considered. Here we investigate if some stable spectral peaks can be associated with "more realistic" shape of intrusions and media structure. We selected two sources: the first located outside the high-scattering region, at $x_A =$

12.5 km and $z_A = 8.0$ km, and the second located in the region of the higher scattering and within a low-velocity intrusion, at $x_B = 12.5$ km and $z_B = 11.4$ km.

The location of two sources and the respective signals and spectra are shown in Figures 7 and 8 for the vertical and horizontal components of the displacement, respectively.

Although all observed spectra contain pronounced spectral peaks, the positions of these peaks vary significantly from one receiver to another. In particular, in spectra computed from whole seismograms, we cannot identify peaks that persist at all receivers. Our interpretation is that these peaks are produced as a result of interference of direct and many scattered waves arriving at receivers. Because the traveling paths of these arrivals are not the same for the different source-receiver configurations, the resulting spectra are different.

An important consequence of this result is that the spectral peaks of signals of volcanic earthquakes located within a very heterogeneous part of magmatic plumbing systems do not directly reflect the processes occurring in the vicinity of the source, but mostly result from the multiple scattering of waves.

However, the "local resonances" are excited by sources located within the highly scattering parts of the media, they might produce long standing coda (B. A. Chouet, 1996). Such long coda might become more "visible" after removing early arrivals, i.e., the ballistic and single scattered waves. Therefore, we investigate the spectra computed from the "late coda". We define its onset as t_s (equation 7) plus 12 seconds (indicated vertical blue line on the seismograms in Figures 7 and 8). The respective amplitude spectra are shown in lower panels of the same Figures.

For source A located relatively far from most heterogeneous parts of the media, we do not see peaks consistently observed at all receivers, either in the spectra computed from the full signals or from the late coda. This is likely explained by absence of "local resonances" in the relatively homogeneous media surrounding source A. In this situation, the peaks in the spectra arise from the multiple scattering occurring relatively far from the source with different interference patterns for each source-receiver configuration.

For source B located in the middle of the largest "scattering bright spot", we still do not see persistent peaks in the spectra computed from the whole signal. Such persistent peaks clearly appear in vertical component spectra (Figure 7) of the late coda at around 1.8, 2.9, and 3.1 Hz. The first of these peaks is also seen in the horizontal component (Figure 8) on four receivers of five. We hypothesize that these spectral peaks are related to the locally resonating waves mentioned above.

To verify this hypothesis, we specifically focus on the peak at 1.8 Hz. We plot in Figure 9 "snapshots" of vertical displacements recorded at receiver 2 and generated by sources distributed along the profile located at $x = 12$ km, with z varying from 2.5 to 14 km and filtered between 1 and 2 Hz.

The first "snapshot" $t = 1.5$ s might be clearly interpreted in the reciprocal sense, when it would represent the displacement recorded at all points distributed along the vertical profile from the source located at the position of receiver 2. With this in mind, we clearly see the ballistic waves propagating downward.

In the later "snapshots" starting from 5.12 s, the ballistic waves disappear and the recorded displacements correspond to scattered waves. Similarly to what has been shown with the simulated wavefield snapshot (Figure 2) and with the analysis of the scattered wave energy (Figure 6), the displacement amplitude maximizes at depths between 10 and 13 km within the highly heterogeneous part of the media. Remarkably, in this most energetic part of the "snapshots" we do not see an upward or downward propagation but

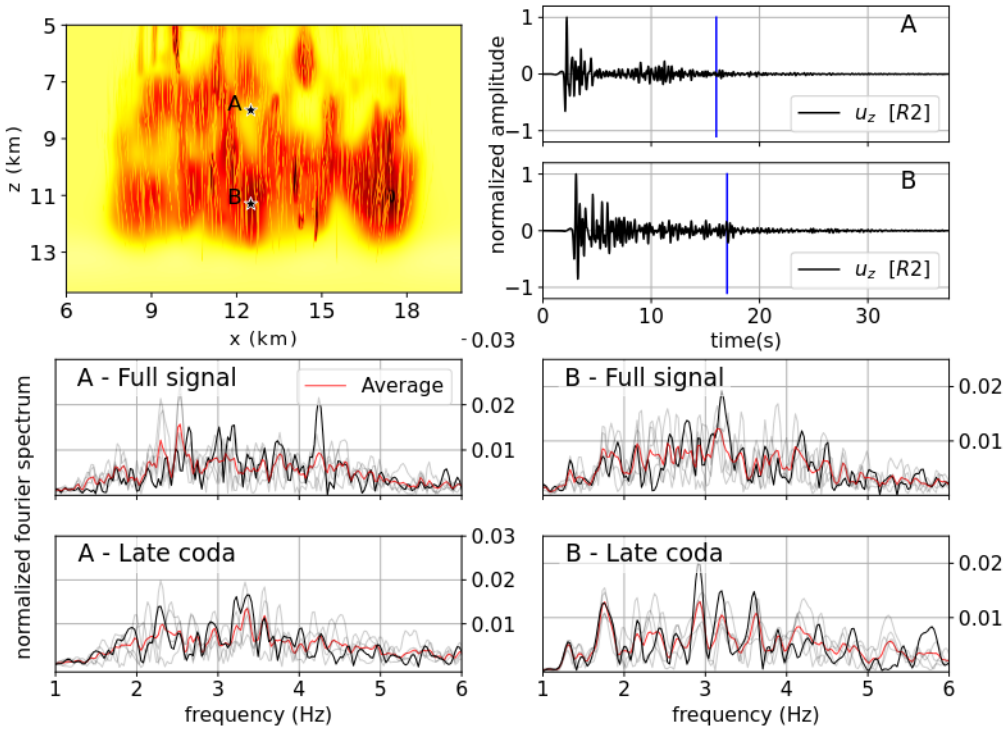

Figure 7. Vertical displacement seismograms and corresponding spectra computed for vertical force sources A and B shown in the upper left frame. Upper right frames show signals at receiver number 2. Middle frames show spectra computed from the whole signal. Lower frames show spectra computed from the “late” coda (onset indicated on seismograms with vertical blue lines. Black lines show spectra at receiver number 2. Light gray lines show spectra at other 4 receivers. Red lines show the average spectra observed at the 5 receivers.

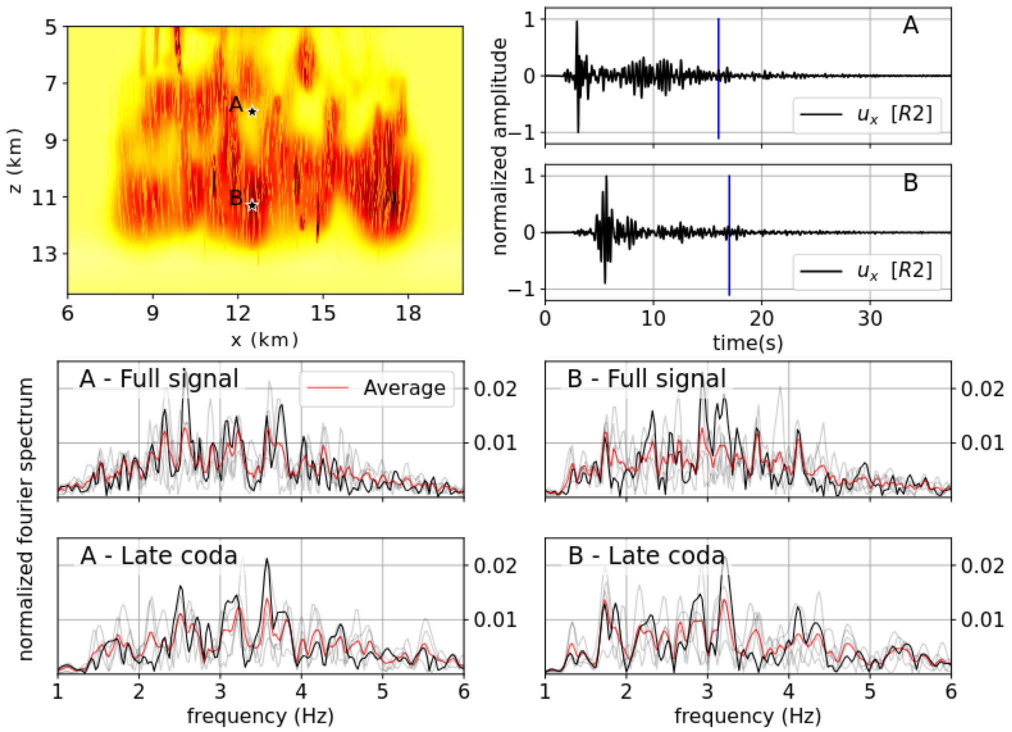

Figure 8. Similar to Figure 7 but for horizontal displacement seismograms.

rather a succession of maxima and nodal points characteristic of standing waves that can be directly associated with the local resonances. The source B is located in the depth range where these standing waves emerge, resulting in a 1.8 Hz peak observed in the late coda. In contrast, source A is not prone to generate such standing waves in the considered frequency range, which explains why no persistent spectral peaks are observed at the surface.

5 Discussion and conclusions

Volcanic edifices and underlying magmatic plumbing systems are known as one of the most heterogeneous parts of the Earth's crust where the propagation of seismic waves is affected by strong scattering expressed in enhanced coda of recorded seismograms (e.g., Wegler & Lühr, 2001; Wegler, 2003; Del Pezzo, 2008; Yamamoto & Sato, 2010; Obermann et al., 2014; Chaput et al., 2015; Blondel et al., 2018). Still, the nature of this strong heterogeneity as well as its strength and spatial distribution remain poorly known. In the absence of knowledge about the real volcanic structure at depth, we tested the seismic signature of a synthetic magmatic system, whose model was built based on modern concepts of magma transport and storage in the Earth's crust (O. E. Melnik et al., 2021). The results of our numerical simulations have implications for the applicability of the "standard" scattering theories, for the interpretation of the spectra of volcanic earthquakes in terms of their source properties, and eventually for the seismo-volcanic monitoring.

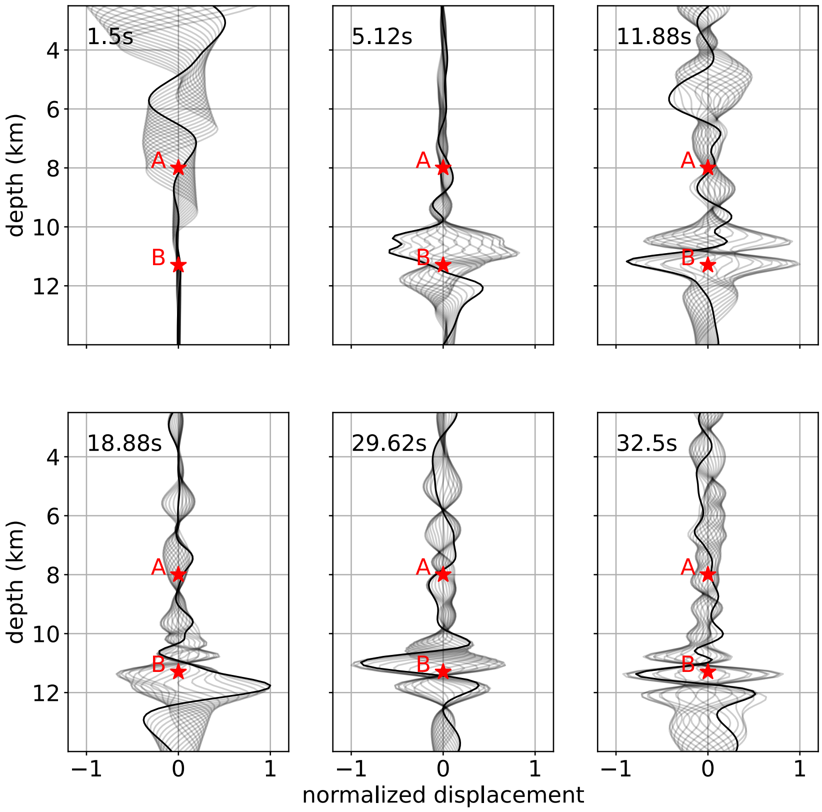

Figure 9. Vertical displacements recorded at receiver 2 and generated by sources distributed along the profile located at $x = 12\,\text{km}$, with z varying from 2.5 to 14 km. The signals are filtered between 1 and 2 Hz. At each subplot, displacements at 20 subsequent times spaced by 0.025 s are shown. The black line corresponds to the time indicated in the plots, and the gray lines for the following 19 time steps. The points marked with stars, A and B, refer to the two sources analyzed in Section 4.2.

5.1 Scattering regime of seismic waves in the strongly heterogeneous plumbing systems.

In seismology, the scattered seismic waves forming the coda of seismograms are most often modeled with the radiative transfer theory (e.g., Margerin et al., 1998; Margerin, 2005; Sato et al., 2012) or its asymptotic cases such the single-scattering and the diffusion approximations (e.g., Aki & Chouet, 1975). In this framework, only the wavefield intensity is accounted for and the phase is ignored. The resulting approach for analyzing the signals consist of measuring the decay of smoothed amplitude envelopes to obtain the coda quality factor Q_c. The idea is that, in statistically uniform media under configuration averaging assumptions, Q_c is simply related to the media intrinsic attenuation and the scattering mean free path. The latter, in turn, can be used to infer statistical description of the media heterogeneity (often based on the Born approximation valid for relatively weak scattering). With a good source-receiver coverage, the observations of the decay of coda envelopes can be regionalized (e.g., Calvet et al., 2013; Mayor et al., 2014). This approach has been also applied in some volcanic regions to obtain maps and spatial distributions of Q_c and separately of scattering coefficients and intrinsic attenuation (De Siena et al., 2014; Del Pezzo et al., 2016).

We note that a necessary condition for applicability of the regionalization based on the radiative transfer is that the media heterogeneity distribution remains uniform over sufficiently extended areas where the statistical scattering parameters can be meaningfully estimated. Additionally, the radiative transfer approximation is valid for a limited range of media fluctuations. When these fluctuations become too strong, the phenomenon of energy localization might become important (e.g., Ryzhik et al., 1996). This localization can be enhanced in strongly anisotropic media with local structure approaching 1D distributions (Asch et al., 1991).

Wave propagation in our physics-based synthetic model has several clear differences from that in statistically uniform scattering models under configuration averaging assumptions. In the physical model that we consider, the medium heterogeneity is primary due to the very strong contrast between the solid rocks and the partially molten magma that has been deposited as intrusions with strongly anisotropic orientation: vertical dikes below 6 km and horizontal sills between 3.5 and 6 km. As a consequence, velocity fluctuations ϵ become very strong ($> 40\%$) in areas dominated by magma injection, as shown in Figure 1. At the same time, the local structure in these parts of the model is highly anisotropic as can be seen from comparing the media correlation lengths compute in horizontal (Figure S3) and vertical (Figure S4) directions.

As shown in Figure 6, the scattering is dominated by these areas that concentrate very strong and anisotropic heterogeneity. In such configuration, the classical quantity used to distinguish scattering regimes: $ka = \frac{\omega}{<V_s>}a$ (where k is the wavenumber, ω is the angular frequency, a is the media correlation length, and $< V_s >$ is the average velocity), seems not being very pertinent. In the most heterogeneous parts of the model the values of ka might be estimated between 0.1 and 1 which could imply strong scattering . However, these estimations do not account for the rapid spatial evolution of the level of local average velocity and depend very strongly on the direction in which the media correlation length is estimated (Figures S5, S6).

Our simulations show that the scattering occurring in the highly heterogeneous intrusion-dominated areas is frequency dependent (Figure 6). This is confirmed by emergence of the locally standing waves in the late coda (Figure 9). Such phenomena clearly cannot be explained without accounting for the wavefield phase, implying that in the considered medium, the validity of the radiative transfer is broken. Therefore, imaging the "realistic" volcanic media might require different approaches than those based on smoothed signal amplitude envelopes. Methods based on the full wave-field (including its phase) might be a better alternative (e.g., De Barros et al., 2012; Blondel et al., 2018; Touma et al., 2023; Giraudat et al., 2024).

5.2 Spectra of volcanic earthquakes: source or multiple scattering path effects?

We analyzed synthetic seismograms and their spectra in relation to the position of the source in the medium. For this purpose, the model of magmatic system was covered by a dense network of sources. While all sources had the same source time function that is characterized by a smooth spectrum (dashed red lines in Figure 3), the synthetic seismograms were characterized by multiple narrow spectral peaks (Figures 3, 7, and 8). An analysis of the signals produced by all the sources shows that these spectral peaks are associated with the coda (Figure 4). Also, central frequencies and amplitudes of most of spectral peaks change when analyzing seismograms from the same source recorded at different receivers (Figures 7 and 8). Overall, this shows that most of the spectral peaks are not due to particular near source processes but emerge because of the interference of many ballistic and scattered arrivals (as has been suggested by Barajas et al. (2023)) with the latter caused by the very strong media heterogeneity.

At the same time, as discussed in subsection 4.2, some spectral peaks seen in the late coda remain stable over multiple receivers and are associated with local "standing waves" excited in the vicinity of the sources located withing strong low velocity anomalies associated with intrusions containing the partially molten magma. Such "local resonances" have similarity with fluid fluid filled crack model (e.g., B. A. Chouet, 1996) often used to interpret the observed spectra of long-period volcanic earthquakes and tremors.

Overall, our results show that most of spectral peaks observed in the seismo-volcanic signals cannot be simply related to the source effects. Most likely, the large majority of these peaks are causes by the multiple scattering of waves within strongly heterogeneous volcanic media. Only most stable of these peaks associated with long-duration coda can be eventually related to the near source features. However, identifying such source-related resonances requires a very careful analysis with comparing signals recorded at different locations and at different components. So far, our simulation results indicate that excitation of particular peaks may change with changing the source radiation pattern (Figures S7 and S8). Additionally, some areas might be prone to resonances observed on vertical components (Figure 7) while others more prone to produce such phenomena at horizontal components (as shown in Figures S9, S10). Finally, semi-analytical formulas based on regular-shaped homogeneous geometries (Maeda & Kumagai, 2013, 2017) can provide only very approximate descriptions of real resonating intrusions.

5.3 Implications for seismo-volcanic monitoring.

Our simulation show that the detailed spectral content of the seismo-volcanic signals is very sensitive to the position of the sources and to the distribution of the heterogeneity (magmatic melt) withing the volcano plumbing systems. Consequently, observed variations in this spectral content can be used to detect the changes either in the internal structure either in the position of the sources. Studying the time varying spectral content can be particularly interesting for continuous seismo-volcanic tremors whose provenance is difficult to determine with accuracy. This is often done with analyzing the spectrograms of the time-frequency representation of the spectral width of the network covariance matrix (e.g., Seydoux et al., 2016; Journeau et al., 2022).

Recently, the time evolution of the spectral content of continuous seismic signals recorded at volcanoes has been studied with the machine learning (ML) approaches. So far, Soubestre et al. (2018) used the eigenvectors of the network covariance matrix to find different clusters of the volcanic tremors corresponding to different episodes of activity of volcanoes of the Klyuchevskoy Volcanic Group in Kamchatka. Steinmann et al. (2024) used a combination of the scattering transform (Seydoux et al., 2020) (a multi-layer time frequency representation of a signal combined with the Uniform manifold approximation and projection (UMAP) (McInnes & Healy, 2018) to observe continuous changes in signals from the same volcanic region during almost one year and to relate them to different phases of pre- and co-eruptive volcanic activity.

The mentioned studies produced empirical clustering of observed seismograms. More advanced interpretation of these results would require understanding the physical origin of the analyzes signals. In particular, this is important to understand if the observed variations of signals should be linked to sources (location, source time function, mechanism) or to changes in the medium. However, such separation is difficult in absence of coda sensitivity kernels in non-uniform media are not yet available (van Dinther et al., 2021).

The physical interpretations of the results of the numerical simulations presented in the present paper suggest that machine learning techniques could help us to interpret the complex actual signals in terms of the heterogeneity of the medium in the region of the source. We test this this possibility in a companion article (Esfahani et al., submitted 2025) where we analyze the seismograms described here with the same combination of scattering transform and UMAP used by Steinmann et al. (2024) for the analysis of real data in Kamchatka. This allows for clustering the synthetic signals from different sources and for differentiating the scattering conditions at the source area.

Open Research

Data availability statement

The dataset associated with this study has been uploaded to Zenodo and is accessible at https://zenodo.org/records/15118518.

Acknowledgments

This work is supported by the European Union's Horizon 2020 research and innovation program under the Marie Skłodowska-Curie grant agreement No 955515 and by The European Research Council under the European Union Horizon 2020 research and innovation program (Grant agreements no 742335, F-IMAGE for M.B. and M.C. and 787399, SEISMAZE for O.M. and N.S.).

References

Abubakirov, I., & Gusev, A. (1990). Estimation of scattering properties of lithosphere of kamchatka based on monte-carlo simulation of record envelope of a near earthquake. *Physics of the Earth and Planetary Interiors*, *64*(1), 52-67. doi: https://doi.org/10.1016/0031-9201(90)90005-I

Aki, K., & Chouet, B. (1975). Origin of coda waves: Source, attenuation, and scattering effects. *Journal of Geophysical Research*, *80*(23), 3322–3342. doi: 10.1029/jb080i023p03322

Aki, K., Fehler, M., & Das, S. (1977). Source mechanism of volcanic tremor: fluid-driven crack models and their application to the 1963 kilauea eruption. *Journal of Volcanology and Geothermal Research*, *2*(3), 259-287. doi: https://doi.org/10.1016/0377-0273(77)90003-8

Aki, K., & Richards, P. G. (2002). *Quantitative seismology* (2nd ed.). University Science Books. Hardcover. Retrieved from `http://www.worldcat.org/isbn/0935702962`

Annen, C., Blundy, J. D., & Sparks, R. S. J. (2005). The genesis of intermediate and silicic magmas in deep crustal hot zones. *Journal of Petrology*, *47*(3), 505-539. doi: 10.1093/petrology/egi084

Asch, M., Kohler, W., Papanicolaou, G., Postel, M., & White, B. (1991). Frequency content of randomly scattered signals. *SIAM Review*, *33*(4), 519-625. doi: 10.1137/1033136

Barajas, A., Journeau, C., Obara, K., & Shapiro, N. M. (2023). Comparison of continuously recorded seismic wavefields in tectonic and volcanic environments based on the network covariance matrix. *Journal of Geophysical Research: Solid Earth*, *128*(12), e2023JB026784. doi: https://doi.org/10.1029/2023JB026784

Bean, C. J., De Barros, L., Lokmer, I., Métaxian, J.-P., O'Brien, G., & Murphy, S. (2014). Long-period seismicity in the shallow volcanic edifice formed from slow-rupture earthquakes. *Nature Geoscience*, *7*(1), 71–75. doi: 10.1038/ngeo2027

Blondel, T., Chaput, J., Derode, A., Campillo, M., & Aubry, A. (2018). Matrix approach of seismic imaging: Application to the erebus volcano, antarctica. *Journal of Geophysical Research: Solid Earth*, *123*(12), 10,936-10,950. doi: https://doi.org/10.1029/2018JB016361

Calvet, M., Sylvander, M., Margerin, L., & Villaseñor, A. (2013). Spatial variations of seismic attenuation and heterogeneity in the pyrenees: Coda q and peak delay time analysis. *Tectonophysics*, *608*, 428-439. doi: https://doi.org/10.1016/j.tecto.2013.08.045

Cao, J., Brossier, R., Górszczyk, A., Métivier, L., & Virieux, J. (2022). 3-d multiparameter full-waveform inversion for ocean-bottom seismic data using an efficient fluid–solid coupled spectral-element solver. *Geophysical Journal International*, *229*(1), 671-703. doi: 10.1093/gji/ggab484

Cashman, K. V., Sparks, R. S. J., & Blundy, J. D. (2017). Vertically extensive and unstable magmatic systems: A unified view of igneous processes. *Science*, *355*(6331), eaag3055. doi: 10.1126/science.aag3055

Chaput, J., Campillo, M., Aster, R. C., Roux, P., Kyle, P. R., Knox, H., & Czoski, P. (2015). Multiple scattering from icequakes at erebus volcano, antarctica: Implications for imaging at glaciated volcanoes. *Journal of Geophysical Research: Solid Earth*, *120*(2), 1129-1141. doi: https://doi.org/10.1002/2014JB011278

Chouet, B. (1986). Dynamics of a fluid-driven crack in three dimensions by the finite difference method. *Journal of Geophysical Research: Solid Earth*, *91*(B14), 13967-13992. Retrieved from `https://agupubs.onlinelibrary.wiley.com/doi/abs/10.1029/JB091iB14p13967` doi: https://doi.org/10.1029/JB091iB14p13967

Chouet, B. (1988). Resonance of a fluid-driven crack: Radiation properties and implications for the source of long-period events and harmonic tremor. *Journal of Geophysical Research: Solid Earth*, *93*(B5), 4375-4400. Retrieved from `https://agupubs.onlinelibrary.wiley.com/doi/abs/10.1029/JB093iB05p04375` doi: https://doi.org/10.1029/JB093iB05p04375

Chouet, B. A. (1996). Long-period volcano seismicity: its source and use in eruption forecasting. *Nature*, *380*, 309-316. doi: 10.1038/380309a0

Chouet, B. A., & Matoza, R. S. (2013). A multi-decadal view of seismic methods for detecting precursors of magma movement and eruption. *J. Volcanol. Geoth. Res.*, *252*, 108–175. doi: 10.1016/j.jvolgeores.2012.11.013

De Barros, L., Martini, F., Bean, C. J., Garcia-Yeguas, A., & Ibáñez, J. (2012). Imaging magma storage below teide volcano (tenerife) using scattered seismic wavefields. *Geophysical Journal International*, *191*(2), 695-706. Retrieved from `https://doi.org/10.1111/j.1365-246X.2012.05637.x` doi: 10.1111/j.1365-246X.2012.05637.x

Del Pezzo, E. (2008). Chapter 13 seismic wave scattering in volcanoes. In *Earth heterogeneity and scattering effects on seismic waves* (Vol. 50, p. 353-371). Elsevier.

Del Pezzo, E., Ibañez, J., Prudencio, J., Bianco, F., & De Siena, L. (2016). Absorption and scattering 2-d volcano images from numerically calculated space-weighting functions. *Geophysical Journal International*, *206*(2), 742-756. doi: 10.1093/gji/ggw171

De Siena, L., Thomas, C., Waite, G. P., Moran, S. C., & Klemme, S. (2014). Attenuation and scattering tomography of the deep plumbing system of mount st. helens. *Journal of Geophysical Research: Solid Earth*, *119*(11), 8223-8238. doi: https://doi.org/10.1002/2014JB011372

Giraudat, E., Burtin, A., Le Ber, A., Fink, M., Komorowski, J.-C., & Aubry, A. (2024). Matrix imaging as a tool for high-resolution monitoring of deep volcanic plumbing systems with seismic noise. *Communications Earth & Environment*, *5*(1), 509. doi: 10.1038/s43247-024-01659-2

Girona, T., Caudron, C., & Huber, C. (2019). Origin of shallow volcanic tremor: The dynamics of gas pockets trapped beneath thin permeable media. *Journal of Geophysical Research: Solid Earth*, *124*(5), 4831-4861. doi: https://doi.org/10.1029/2019JB017482

Iverson, R. M., Dzurisin, D., Gardner, C. A., Gerlach, T. M., LaHusen, R. G., Lisowski, M., … Vallance, J. W. (2006). Dynamics of seismogenic volcanic extrusion at mount st helens in 2004–05. *Nature*, *444*(7118), 439–443. doi: 10.1038/nature05322

Jellinek, A. M., & Bercovici, D. (2011). Seismic tremors and magma wagging during explosive volcanism. *Nature*, *470*(7335), 522–525. doi: 10.1038/nature09828

Journeau, C., Shapiro, L., N. M.and Seydoux, Soubestre, J., Koulakov, I. Y., Jakovlev, A. V., Abkadyrov, I., … Jaupart, C. (2022). Seismic tremor reveals active trans-crustal magmatic system beneath Kamchatka volcanoes. *Sci. Adv.*, *8*(5), eabj1571. doi: 10.1126/sciadv.abj1571

Julian, B. R. (1994). Volcanic tremor: Nonlinear excitation by fluid flow. *Journal of Geophysical Research: Solid Earth*, *99*(B6), 11859-11877. doi: https://doi.org/10.1029/93JB03129

Komatitsch, D., & Vilotte, J.-P. (1998). The spectral element method: An efficient tool to simulate the seismic response of 2d and 3d geological structures. *Bulletin of the Seismological Society of America*, *88*(2), 368-392. doi: 10.1785/BSSA0880020368

Koulakov, I., & Shapiro, N. (2014). Seismic tomography of volcanoes. In M. Beer, I. A. Kougioumtzoglou, E. Patelli, & I. S.-K. Au (Eds.), *Encyclopedia of earthquake engineering* (pp. 1–18). Berlin, Heidelberg: Springer Berlin Heidelberg. doi: 10.1007/978-3-642-36197-5_51-1

Maeda, Y., & Kumagai, H. (2013). An analytical formula for the longitudinal resonance frequencies of a fluid-filled crack. *Geophysical Research Letters*, *40*(19), 5108-5112. doi: https://doi.org/10.1002/grl.51002

Maeda, Y., & Kumagai, H. (2017). A generalized equation for the resonance frequencies of a fluid-filled crack. *Geophysical Journal International*, *209*(1), 192-201. doi: 10.1093/gji/ggx019

Margerin, L. (2005). Introduction to radiative transfer of seismic waves. In *Seismic earth: Array analysis of broadband seismograms* (p. 229-252). American Geophysical Union (AGU). doi: https://doi.org/10.1029/157GM14

Margerin, L., Campillo, M., & Tiggelen, B. (1998). Radiative transfer and diffusion of waves in a layered medium: new insight into coda Q. , *134*(2), 596-612. doi: 10.1111/j.1365-246X.1998.tb07142.x

Matoza, R. S., & Chouet, B. A. (2010). Subevents of long-period seismicity: Implications for hydrothermal dynamics during the 2004–2008 eruption of mount st. helens. *Journal of Geophysical Research: Solid Earth*, *115*(B12). doi:

https://doi.org/10.1029/2010JB007839

Mayor, J., Margerin, L., & Calvet, M. (2014). Sensitivity of coda waves to spatial variations of absorption and scattering: radiative transfer theory and 2-d examples. *Geophysical Journal International*, *197*(2), 1117-1137. doi: 10.1093/gji/ggu046

McInnes, L., & Healy, J. (2018). UMAP: Uniform manifold approximation and projection for dimension reduction. *arXiv preprint arXiv:1802.03426*. Retrieved from `https://arxiv.org/abs/1802.03426`

Melnik, O., Lyakhovsky, V., Shapiro, N., Galina, N., & Bergal-Kuvikas, O. (2020). Deep long period volcanic earthquakes generated by degassing of volatile-rich basaltic magmas. *Nature Communications*, *11*(1), 3918.

Melnik, O., Lyakhovsky, V., & Shapiro, N. M. (2024). Rapid gas bubble growth in basaltic magma as a source of deep long period volcanic earthquakes. *Journal of Geophysical Research: Solid Earth*, *129*(11), e2024JB029602. doi: https://doi.org/10.1029/2024JB029602

Melnik, O. E., Utkin, I. S., & Bindeman, I. N. (2021). Magma chamber formation by dike accretion and crustal melting: 2d thermo-compositional model with emphasis on eruptions and implication for zircon records. *Journal of Geophysical Research: Solid Earth*, *126*(12), e2021JB023008. Retrieved from `https://agupubs.onlinelibrary.wiley.com/doi/abs/10.1029/2021JB023008` (e2021JB023008 2021JB023008) doi: https://doi.org/10.1029/2021JB023008

Obermann, A., Larose, E., Margerin, L., & Rossetto, V. (2014). Measuring the scattering mean free path of rayleigh waves on a volcano from spatial phase decoherence. *Geophysical Journal International*, *197*(1), 435-442. doi: 10.1093/gji/ggt514

Ripperger, J., Igel, H., & Wasserman, J. (2003). Seismic wave simulation in the presence of real volcano topography. *Journal of Volcanology and Geothermal Research*, *128*(1), 31-44. Retrieved from `https://www.sciencedirect.com/science/article/pii/S0377027303002452` (Putting Volcano Seismology in a Physical Context. In memory of Bruno Martinelli) doi: https://doi.org/10.1016/S0377-0273(03)00245-2

Ryzhik, L., Papanicolaou, G., & Keller, J. B. (1996). Transport equations for elastic and other waves in random media. *Wave Motion*, *24*(4), 327-370. doi: https://doi.org/10.1016/S0165-2125(96)00021-2

Sato, H., Fehler, M., & Maeda, T. (2012). *Seismic wave propagation and scattering in the heterogeneous earth: Second edition.* Springer Berlin, Heidelberg. doi: 10.1007/978-3-642-23029-5

Schmeling, H., Kruse, J. P., & Richard, G. (2012). Effective shear and bulk viscosity of partially molten rock based on elastic moduli theory of a fluid filled poroelastic medium. *Geophysical Journal International*, *190*(3), 1571-1578. doi: 10.1111/j.1365-246X.2012.05596.x

Seydoux, L., Balestriero, R., Poli, P., de Hoop, M., Campillo, M., & Baraniuk, R. (2020). Clustering earthquake signals and background noises in continuous seismic data with unsupervised deep learning. *Nature Communications*, *11*(1), 3972. Retrieved from `https://doi.org/10.1038/s41467-020-17841-x` (Published: 2020/08/07) doi: 10.1038/s41467-020-17841-x

Seydoux, L., Shapiro, N., de Rosny, J., Brenguier, F., & Landès, M. (2016). Detecting seismic activity with a covariance matrix analysis of data recorded on seismic arrays. *Geophysical Journal International*, *204*(3), 1430–1442. doi: 10.1093/gji/ggv531

Soubestre, J., Shapiro, N. M., Seydoux, L., de Rosny, J., Droznin, D. V., Droznina, S. Y., . . . Gordeev, E. I. (2018). Network-based detection and classification of seismovolcanic tremors: Example from the Klyuchevskoy Volcanic Group in Kamchatka. *Journal of Geophysical Research: Solid Earth*, *123*(1), 564–582. doi: 10.1002/2017JB014726

Steinmann, R., Seydoux, L., Journeau, C., Shapiro, N. M., & Campillo, M. (2024). Machine learning analysis of seismograms reveals a continuous plumbing system evolution beneath the klyuchevskoy volcano in kamchatka, russia. *Journal of Geophysical Research: Solid Earth*, *129*(3), e2023JB027167. Retrieved from https://agupubs.onlinelibrary.wiley.com/doi/abs/10.1029/2023JB027167 (e2023JB027167 2023JB027167) doi: https://doi.org/10.1029/2023JB027167

Touma, R., Le Ber, A., Campillo, M., & Aubry, A. (2023). Imaging the crustal and upper mantle structure of the north anatolian fault: A transmission matrix framework for local adaptive focusing. *Journal of Geophysical Research: Solid Earth*, *128*(11), e2023JB026704. doi: https://doi.org/10.1029/2023JB026704

Trinh, P., Brossier, R., Lemaistre, L., Métivier, L., & Virieux, J. (2019). 3d elastic fwi with a non-linear model constraint: Application to a real complex onshore dataset. , *2019*(1), 1-5. doi: https://doi.org/10.3997/2214-4609.201901344

van Dinther, C., Margerin, L., & Campillo, M. (2021). Implications of laterally varying scattering properties for subsurface monitoring with coda wave sensitivity kernels: Application to volcanic and fault zone setting. *Journal of Geophysical Research: Solid Earth*, *126*(12), e2021JB022554. Retrieved from https://agupubs.onlinelibrary.wiley.com/doi/abs/10.1029/2021JB022554 (e2021JB022554 2021JB022554) doi: https://doi.org/10.1029/2021JB022554

Wegler, U. (2003). Analysis of multiple scattering at vesuvius volcano, italy, using data of the tomoves active seismic experiment. *Journal of Volcanology and Geothermal Research*, *128*, 45-63. doi: 10.1016/S0377-0273(03)00246-4

Wegler, U., & Lühr, B. G. (2001). Scattering behaviour at merapi volcano (java) revealed from an active seismic experiment. *Geophysical Journal International*, *145*(3), 579-592. doi: 10.1046/j.1365-246x.2001.01390.x

Yamamoto, M., & Sato, H. (2010). Multiple scattering and mode conversion revealed by an active seismic experiment at asama volcano, japan. *Journal of Geophysical Research: Solid Earth*, *115*(B7), B07304. doi: https://doi.org/10.1029/2009JB007109

Supporting Information for "Multiple scattering of seismic waves in a heterogeneous magmatic system and spectral characteristic of long period volcanic earthquakes."

Mirko Bracale[1],Michel Campillo[1], Nikolai M. Shapiro[1], Romain Brossier[1],

Oleg Melnik[2]

[1]ISTerre, Université Grenoble Alpes, CNRS, Université Savoie Mont Blanc, IRD, Université Gustave Eiffel, Grenoble, France

[2]Department of Earth Sciences, University of Oxford, Oxford, UK

Contents of this file

Text S1. Validation of numerical simulations

The validation of the simulations required two analyses, which we outline below: assessment of the effect of absorbing boundaries and verification of compliance with reciprocity.

To assess the effect of absorbing boundaries, we conducted three simulations in a homogeneous medium having the same size as the original model, each lasting 12.5 seconds, progressively increasing the thickness of the absorbing boundaries from 0.1 to 4.5 kilometers. In these simulations, a source was placed at the surface, position (x_s, z_s), while a single receiver was positioned at depth at (x_r, z_r), where $x_r = x_s$. By using a source characterized by vertical force, we aimed to examine the impact of reflections on the edges of the medium by observing the horizontal component of motion at the receiver. In the case of perfect absorption, one would expect a null signal on the horizontal component of the displacement. However, the presence of any signal in this case would indicate the generation of reflections at the edges of the medium.

Analysis of the recorded signal and its spectrum showed the influence of the medium's size. Notably, when employing an absorbing boundary with a thickness of 4.5 kilometers, the recorded signal exhibited energy at frequencies lower than 1 Hz, figure S1. This observation aligns with expectations, as lower frequencies, corresponding to longer wavelengths, experience less attenuation.

The verification of reciprocity involved performing two seismic simulations in which the positions of the source and receiver were exchanged. These simulations used only a single receiver and a single seismic source. Remarkably, the recorded signals in both cases were perfectly identical, figure S2, highlighting the good precision of the computation, even for long lapse time.

Text S2. Correlation length of the medium

The correlation length of the medium was computed by analyzing square regions of the S-velocity model, each measuring 1 km per side. Within each selected region, horizontal and vertical slices were extracted, and their autocorrelation was calculated. The positive values of the autocorrelation were then fitted to an exponential function of the form:

$$f(x) = e^{-x/b} \tag{1}$$

where x denotes the coordinate of the autocorrelation vector, and b is the correlation length to be fitted. Vertical and horizontal sections were analyzed separately, with the final value obtained by averaging the computed values in each square area. The results of this computation are presented in Figure S3, for the horizontal direction, and Figure S4, for the vertical direction.

Text S3. Computation of ka

In scattering theory, the product of the correlation length a and the wave vector $k = 2\pi f$ plays a fundamental role in the determination of the scattering efficiency, and thus the transition between scattering regimes. The calculation of ka presented in this section was performed using the previously determined correlation length and considering the frequency of 3.5 Hz. The results, are shown in Figure S5, using the correlation length computed in the horizontal direction and S6 in the vertical direction.

Text S4. Analysis of seismogram and spectra generated by horizontal force source

This paragraph presents the figures of the seismograms and the spectra observed at receiver number two, generated by two sources located at $x_s = 12.5$km and $z_s = 8$km, source A, and $x_s = 12.5$km and $z_s = 11.4$km, source B. This figure reflects the analysis discussed in paragraph 4.2, but instead of a source expressed by a vertical force, it considers a horizontal force. The horizontal displacement component is shown in Figure S8, while the vertical component is displayed in Figure S7.

Text S5. Analysis of seismogram and spectra generated by vertical force source in a dyke

In paragraph 5.2, we discuss frequency peaks observed in the vertical component of displacement, generated by a vertical force. We show how some stable peaks may be related to the presence of resonances in the medium. In this paragraph, we analyze the spectra of a single source located in a Dyke, at $x_s = 11.5\,\mathrm{km}$ and $z_s = 10\,\mathrm{km}$. The goal of this analysis is to show that stable peaks can appear on any of the two components. In this case, for instance, a common peak for all receivers is visible in the horizontal component 1.8 Hz, Figure S9, while in the vertical component, no clear common peaks are visible, Figure S10.

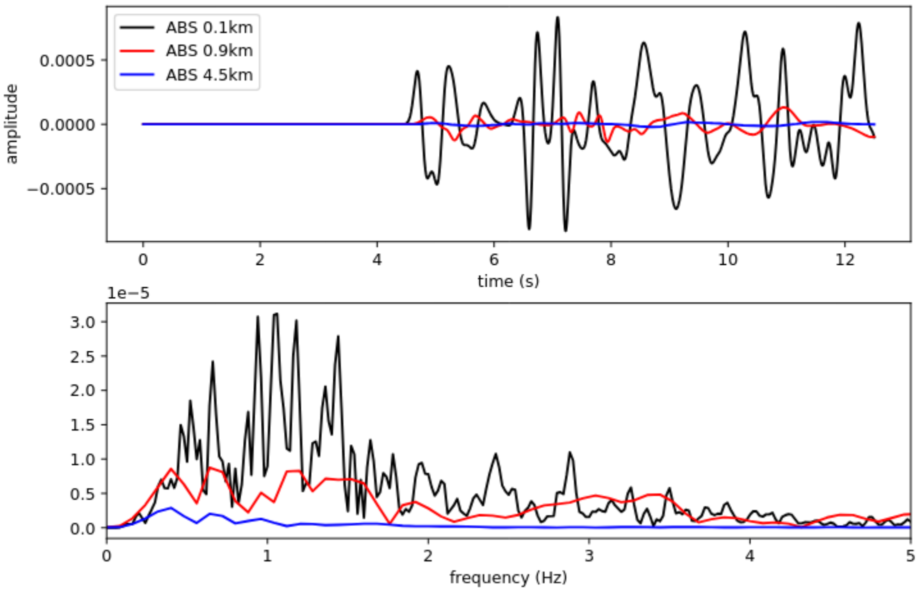

Figure S1. Absorbing boundaries, ABS, test. As the thickness of the absorbing boundaries increases, the reflections from the edge of the medium increase. Using ABS of 4.5km, generates small signals at frequency lower than 1Hz.

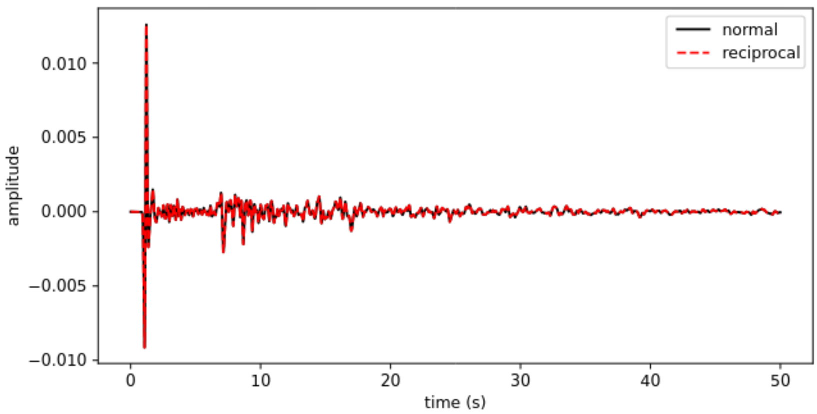

Figure S2. Reciprocity test: the black line represents the simulation where the source was placed at a depth of 2.5 km and the receiver at the surface. The red line was obtained by interchanging the positions.

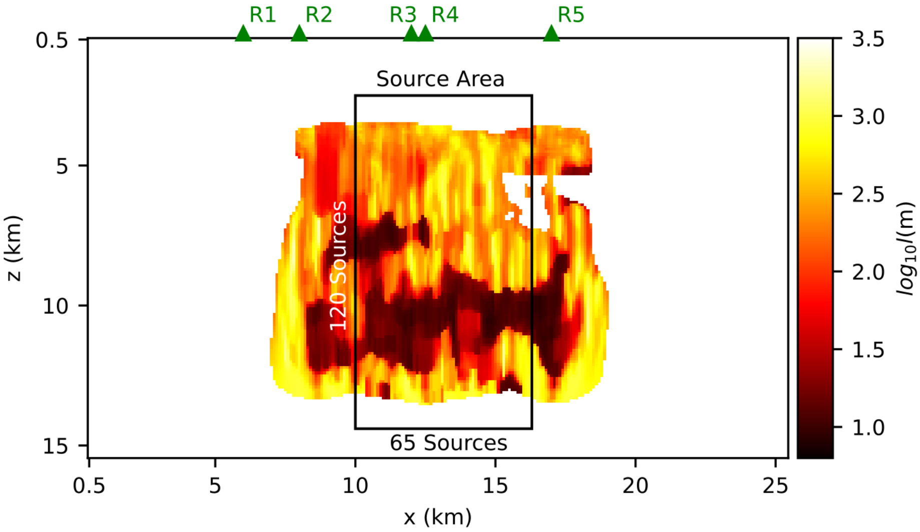

Figure S3. Media correlation length computed in the horizontal direction over segments of 1 km length. Results are only shown for locations where the standard deviation of velocity fluctuations exceeds 5%.

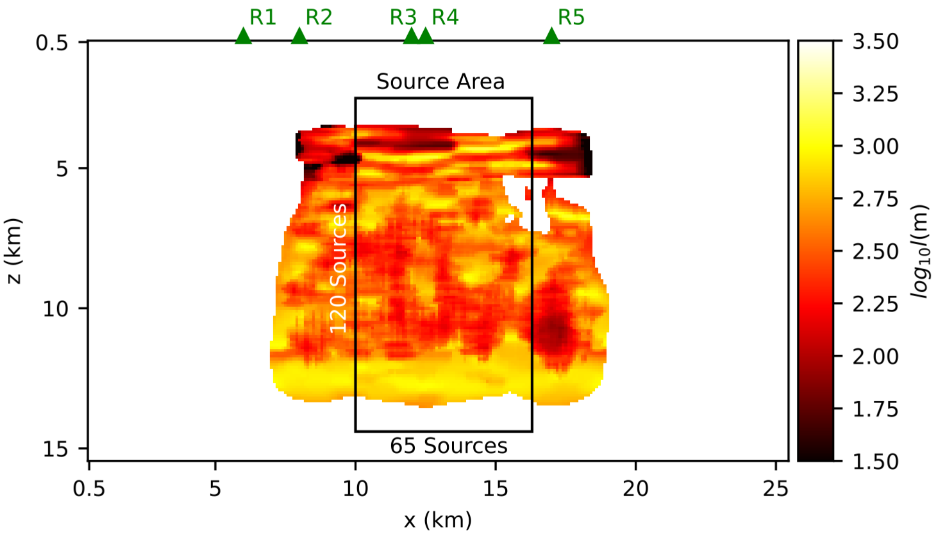

Figure S4. Media correlation length computed in the vertical direction over segments of 1 km length. Results are only shown for locations where the standard deviation of velocity fluctuations exceeds 5%.

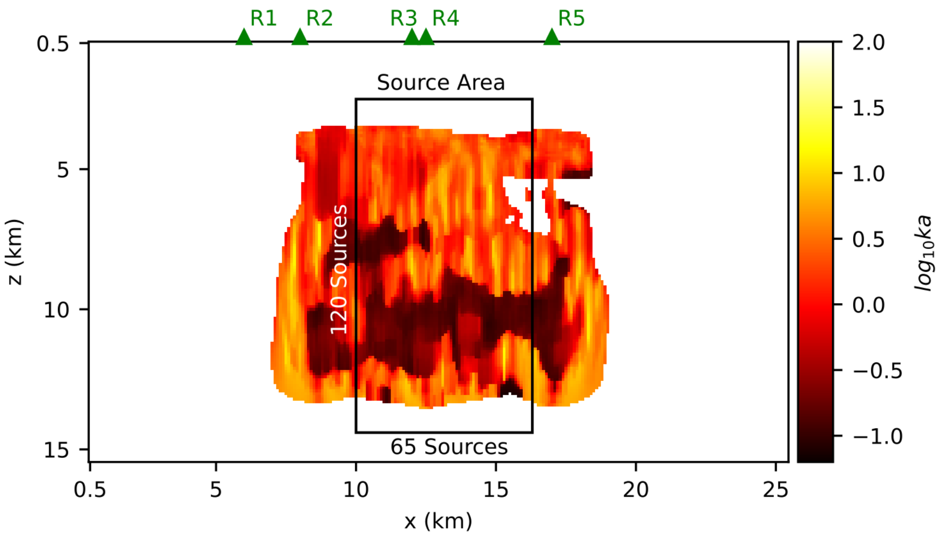

Figure S5. Parameter $ka = \frac{\omega}{<V_s>}a$ estimated at 3 Hz with media correlation length a computed in the horizontal direction over segments of 1 km length and velocity averaged in 1x1 km squares. Results are only shown for locations where the standard deviation of velocity fluctuations exceeds 5%.

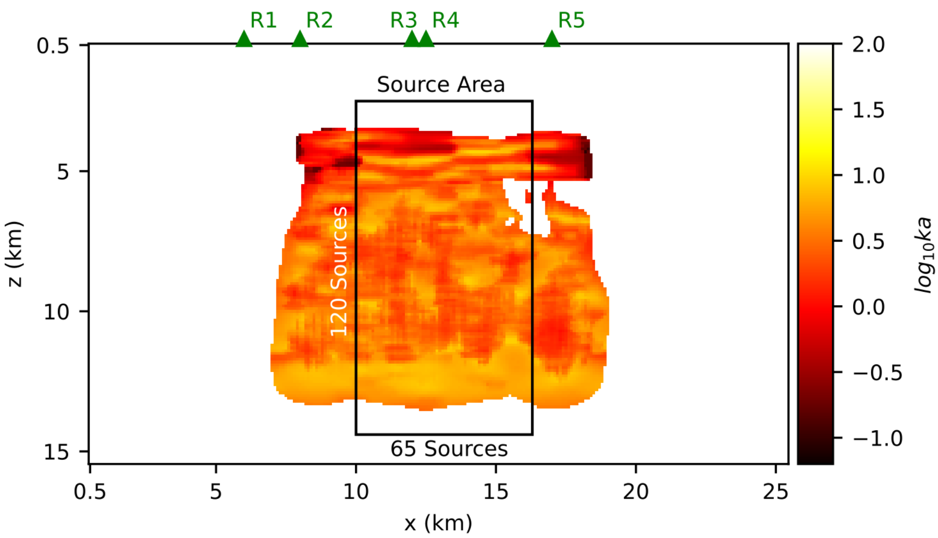

Figure S6. Parameter $ka = \frac{\omega}{<V_s>}a$ estimated at 3 Hz with media correlation length a computed in the vertical direction over segments of 1 km length and velocity averaged in 1x1 km squares. Results are only shown for locations where the standard deviation of velocity fluctuations exceeds 5%.

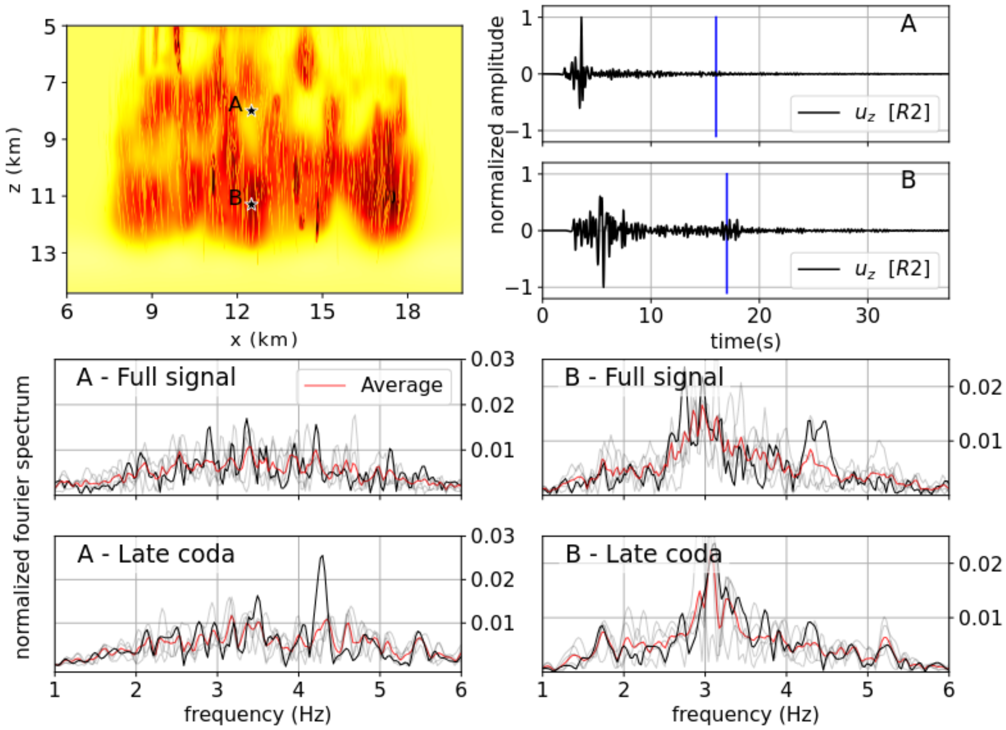

Figure S7. Vertical displacement seismograms and corresponding spectra computed for horizontal force sources A and B shown in the upper left frame. Upper right frames show signals at receiver number 2. Middle frames show spectra computed from the whole signal. Lower frames show spectra computed from the "late" coda (onset indicated on seismograms with vertical blue lines. Black lines show spectra at receiver number 2. Light gray lines show spectra at other 4 receivers. Red lines show the average spectra observed at the 5 receivers.

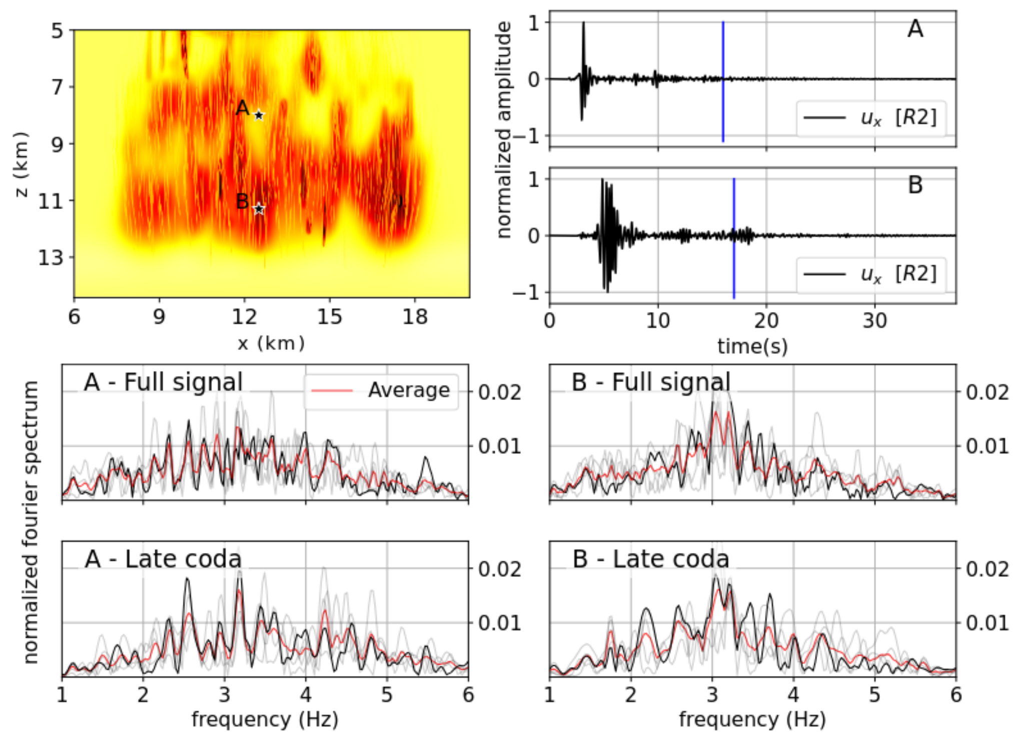

Figure S8. Horizontal displacement seismograms and corresponding spectra computed for horizontal force sources A and B shown in the upper left frame. Upper right frames show signals at receiver number 2. Middle frames show spectra computed from the whole signal. Lower frames show spectra computed from the "late" coda (onset indicated on seismograms with vertical blue lines. Black lines show spectra at receiver number 2. Light gray lines show spectra at other 4 receivers. Red lines show the average spectra observed at the 5 receivers.

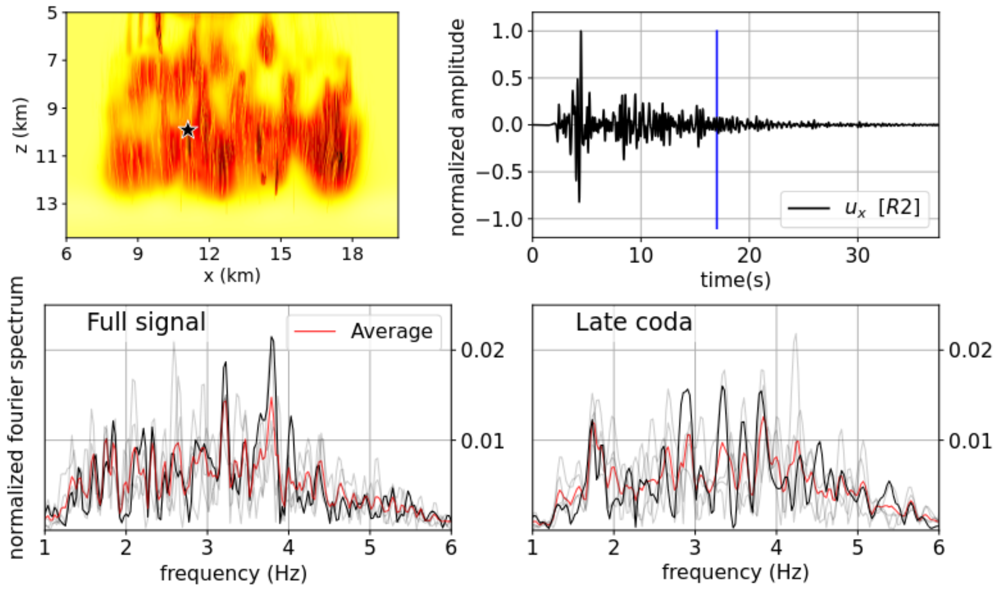

Figure S9. Horizontal displacement seismogram and corresponding spectra computed for horizontal force source shown in the upper left frame. Upper right frame shows signal at receiver number 2. Low frames show spectra computed from the whole signal nd the "late" coda (onset indicated on the seismogram with vertical blue lines. Black lines show spectra at receiver number 2. Light gray lines show spectra at other 4 receivers. Red lines show the average spectra observed at the 5 receivers.

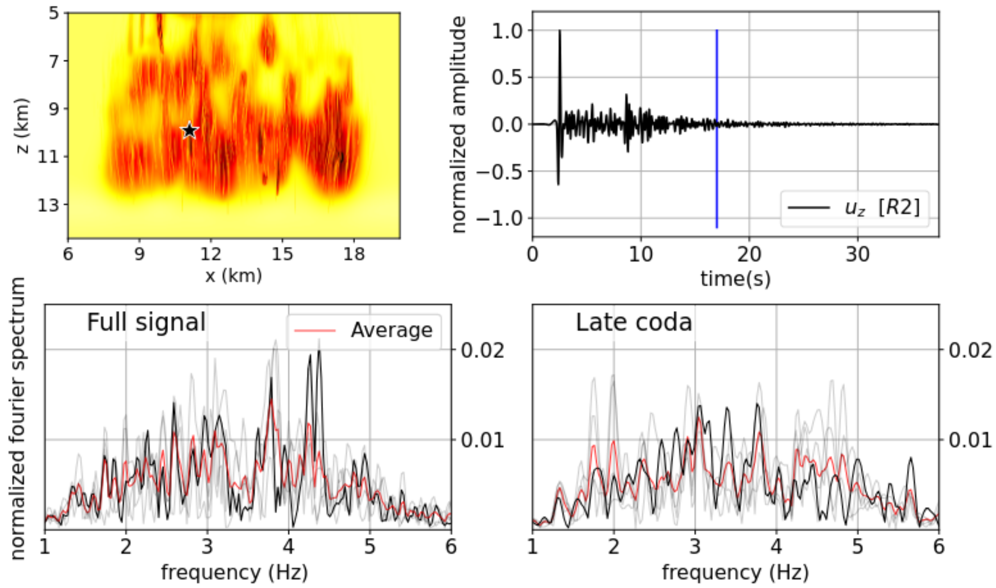

Figure S10. Vertical displacement seismogram and corresponding spectra computed for horizontal force source shown in the upper left frame. Upper right frame shows signal at receiver number 2. Low frames show spectra computed from the whole signal nd the "late" coda (onset indicated on the seismogram with vertical blue lines. Black lines show spectra at receiver number 2. Light gray lines show spectra at other 4 receivers. Red lines show the average spectra observed at the 5 receivers.